International Journal of Thermal Sciences 48 (2009) 2309–2322

Contents lists available at ScienceDirect

International Journal of Thermal Sciences

journal homepage: www.elsevier.com/locate/ijts

Geometric optimization of a thermoacoustic regenerator

Florian Zink [a,*], Hamish Waterer [b], Rosalind Archer [b], Laura Schaefer [c]

[a] University of Pittsburgh, Department of Mechanical Engineering and Material Science, 565 Benedum Hall, Pittsburgh, PA 15261, USA
[b] University of Auckland, Department of Engineering Science, Private Bag 92019, Auckland 1142, New Zealand
[c] University of Pittsburgh, Department of Mechanical Engineering and Material Science , 643 Benedum Hall, Pittsburgh, PA 15261, USA

ARTICLE INFO

Article history:
Received 27 October 2008
Received in revised form
12 March 2009
Accepted 23 May 2009
Available online 24 June 2009

Keywords:
Thermoacoustics
Finite element modeling
Optimization
Nelder–Mead simplex

ABSTRACT

This work illustrates the optimization of thermoacoustic systems, while taking into account thermal losses to the surroundings that are typically disregarded. A simple thermoacoustic engine is used as an example for the methodology. Its driving component, the thermoacoustic regenerator (also referred to as the stack), is modeled with a finite element method and its dimensions are varied to find an optimal design with regard to thermal losses. Thermoacoustic phenomena are included by considering acoustic power, and viscous and capacitive losses that are characteristic for the regenerator. The optimization considers four weighted objectives and is conducted with the Nelder–Mead Simplex method. When trying to minimize thermal losses, the presented results show that the regenerator should be designed to be as short as possible. It was found that there is an optimal regenerator diameter for a given length. The results are presented for a variety of materials and weights for each objective.

1. Introduction

This work shows how the principles of optimization can aid in the design process of thermoacoustic devices. Thermoacoustic devices utilize sound waves to drive a thermodynamic process instead of mechanical pistons. Their advantage is the inherent mechanical simplicity. While the concept is not new, the technology has not been advanced to a high degree, as compared to, for example, the internal combustion engine. Specifically, optimization has not been utilized well as a design tool. Rather, designs of thermoacoustic devices rely on parametric studies and "rule-of-thumb" experience. In this context, optimization will be defined as modeling the entire system and allowing all degrees of freedom to be varied as part of the investigation, as opposed to the parametric study, where only one parameter is varied while all others are kept constant. Before elaborating of the optimization of a thermoacoustic device, we will first introduce the concepts of thermoacoustics in detail. This will also illustrate some of the terminology used in the sections discussing the model, the objective functions and the results.

The basic thermodynamic cycle occurring in thermoacoustic devices is the Stirling cycle, which was developed in 1816 [1]. The original mechanical Stirling engine utilized two pistons and a regenerative heat exchanger [2]. Over the course of one cycle, the working gas is compressed, and it then transfers thermal energy to the heat sink, thus maintaining a constant temperature. Afterwards, the gas is heated at constant volume by the regenerator and then is heated further at the heat source. This heat supply occurs while the gas is allowed to expand and drive the power piston, again at constant temperature. After expansion, the gas is displaced to the heat sink, while cooling off at constant volume by depositing heat to the regenerator, which stores heat between cycle segments [2]. It is noteworthy that this externally heated, closed cycle uses the same gas for all stages, as opposed to the internal combustion engine, which has a constant throughput of working gas and fuel. The first application of this cycle as a thermoacoustic technology occurred when Ceperley recognized that sound waves could replace pistons for gas compression and displacement [3]. Since then, a wide variety of thermoacoustic engines (TAEs) and their counterpart, thermoacoustic refrigerators (TARs), have been developed. Engines utilize a heat input to create intense sound output, while refrigerators can utilize this intense sound to withdraw energy form their surroundings.

1.1. Thermoacoustic engines

There are two main approaches to thermoacoustic engines, namely standing wave and traveling wave devices. Both contain a regenerative unit (called a stack or regenerator, respectively)

* Corresponding author.
E-mail address: flz2@pitt.edu (F. Zink).

1290-0729/$ – see front matter © 2009 Elsevier Masson SAS. All rights reserved.
doi:10.1016/j.ijthermalsci.2009.05.007

Nomenclature

A	area (m^2)
c	speed of sound ($m\,s^{-1}$)
C	capacitance (m^{-1})
c_p	heat capacity ($J\,kg^{-1}\,K^{-1}$)
f	frequency (s^{-1})
g	gravitational acceleration
h	heat transfer coefficient ($W\,m^{-2}\,K^{-1}$)
H	height (m)
k_B	Boltzmann constant
k	thermal conductivity ($W\,m^{-1}\,K^{-1}$)
l	plate thickness (m)
L	inertance ($kg\,m^{-4}$), length (m)
N	number of
p	pressure ($N\,m^{-2}$)
Q	heat flux (W)
R	resistance ($kg\,m^{-2}\,s^{-1}$)
T	temperature (K, °C)
u	velocity ($m\,s^{-1}$)
W	acoustic work (W)
y	plate spacing (m)

Greek symbols

δ	penetration depth (m)
ε	surface emissivity coefficient
ε	plate heat capacity ratio
γ	isentropic coefficient
Γ	temperature gradient ratio
ρ	density ($kg\,m^{-3}$)
ω	angular frequency (s^{-1})
Π	perimeter (m)
∇T	temperature gradient ($K\,m^{-1}$)

Dimensionless groups

Gr	Grashof number
Nu	Nusselt number
Pr	Prandtl number
Ra	Rayleigh number

Subscripts and superscripts

1	first order
∞	ambient, free stream
c	channel
char	characteristic
crit	critical
cold	cold side
cond	conductive
conv	convective
D	diameter
hot	hot side
κ	thermal
m	time averaged
obj	objective
rad	radiative
s	solid, standing
xx,xy,yx,yy	tensor directions
ν	viscous
w	wall

sandwiched between two heat exchangers, one to supply heat at high temperature (on the order of several hundred degrees Celsius), the other to withdraw heat from the system at (ideally) ambient temperature. In practice, the cold side has to be cooled because of conduction of heat from the hot side to the cold side, thus heating this side to temperatures higher than ambient. The temperature gradient across this porous section results in amplification of pressure disturbances in the working gas and results in a loud noise being emitted once a steady state has been achieved. In order for amplification to occur, this temperature gradient has to be larger than the critical temperature gradient, which is related to the temperature gradient that the gas would experience if it were under the influence of a sound wave in adiabatic conditions. The expression for this critical temperature gradient was derived by Swift [4] and is given in Equation (1.1):

$$\nabla T_{\mathrm{crit}} = \frac{\omega p_1^{\mathrm{s}}}{\rho_{\mathrm{m}} c_p u_1^{\mathrm{s}}} \tag{1.1}$$

This critical temperature gradient depends on the operating frequency ω, the first order pressure and velocity in the standing wave p_1^{s} and u_1^{s}, as well as the mean gas density ρ_{m} and specific heat c_p. Depending on the ratio of the temperature gradient and critical temperature gradient, acoustic work is either created (a thermoacoustic engine) when $\frac{\mathrm{d}T/\mathrm{d}x}{\mathrm{d}T/\mathrm{d}x|_{\mathrm{crit}}} > 1$ or transformed into heat energy (a refrigerator) when $\frac{\mathrm{d}T/\mathrm{d}x}{\mathrm{d}T/\mathrm{d}x|_{\mathrm{crit}}} < 1$ [5]. Fig. 1 shows a demonstration engine. It is a standing wave, quarter-wavelength device. The porous stack is located near the closed end of the resonance tube which is the pressure antinode and the velocity node. As a result, the gas inside the stack experiences large pressure oscillations and relatively small displacement. The heat input is provided with a heating wire. Active cooling with a second heat exchanger is not necessary because of the low thermal conductivity of the ceramic regenerative unit.

The phasing of a standing wave is such that pressure and velocity are out of phase, and as a consequence, the heat transfer between the gas and the wall has to be delayed artificially. This delay is achieved by utilizing the poor thermal contact between gas and solid. As a result, however, this heat transfer also causes significant entropy generation, which limits efficiency. In order to avoid these losses, practical device designs have utilized traveling wave phasing, where velocity and pressure are in phase. In this case, the thermal contact between gas and solid does not have to be delayed; the efficiency of such traveling wave devices is inherently better than that of standing wave devices. This traveling wave phasing between pressure and velocity can be achieved in several ways. For example, one can use a looped tube as the compliance or

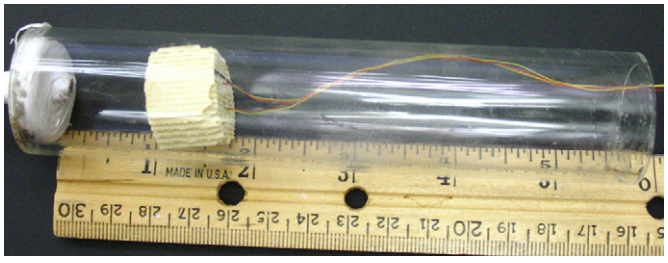

Fig. 1. Picture of a simple standing wave engine demonstrator.

one can utilize an annular so-called feedback inertance. The looped tube is illustrated by Swift in [6]. The latter has been utilized by Bastyr et al. (refer to [7] and [8]) and is very similar to a standing wave device in appearance. Both create a shift in the phase of the pressure wave relative to the velocity wave so that they are actually in phase with each other. This allows for the maximum displacement to occur at the moment of greatest compression or rarefaction, which is advantageous to the underlying thermodynamic cycle. Backhaus et al. introduced a large scale traveling wave engine that achieved a thermal efficiencies of 30%, corresponding to 41% of Carnot efficiency [9]. In any device, the resonator determines the operating frequency [10].

To illustrate the thermoacoustic phenomenon, we can draw parallels to optics. The amplification of the acoustic wave is similar to an optical laser, where light waves travel between a mirror and a partially silvered mirror in a standing wave fashion. The light waves are amplified through resonance and released through the partially mirrored side as a high power laser beam. Similarly, the amplified sound waves can also be extracted from the resonance tube to power external devices [11]. Commonly, the only application of thermoacoustic engines is to drive TARs, which utilize the reverse Stirling cycle, that attenuate the pressure in a sound wave to withdraw heat from the surroundings.

1.2. Thermoacoustic refrigerators without moving parts

Refrigerators and chillers driven by TAEs are a reality today; however they are limited to few, specialized uses, such as gas liquefaction. There are several advanced models of TARs used for these specialized applications. Radebaugh at the National Institute of Standards and Technology (NIST) built a TAR with 5 W of cooling power at 120 K and a low temperature at no load of 90 K [12]. The main benefit is the lack of moving parts (such as seals), thus reducing maintenance costs. It is noteworthy that TARs can achieve these low temperatures in a single stage, whereas conventional vapor compression refrigerators (VCRs) can only achieve approximately 230 K in a single stage [12]. Cryogenic cooling is not the only application for TARs. A practical example of this design was given by Poese with a freezer for ice cream storage. This small scale chiller featured an annular space around the regenerative unit to achieve traveling wave phasing [8]. To date, the applications of thermoacoustics to the field of refrigeration has been very limited, while the advantages have been demonstrated. In addition to the mechanical advantages, TARs do not use harmful refrigerants and can be driven by waste heat. The former is important with respect to the environmental concerns of refrigeration in general, while the latter is an important aspect when refrigeration has to be provided in locations where electrical power is not available or could be conserved. Consider, for example, the air-conditioning system in a passenger vehicle. The engine gives off large amounts of waste heat at high temperature, which could be utilized by a TAR instead of a mechanical air-conditioning system. The result is reduced fuel consumption because the TAR based system does not require pumps or compressors.

1.3. Previous optimization efforts

Currently, thermoacoustic technology is not as advanced as the internal combustion engine, which has experienced significant improvement since its conception over a century ago. As a result, there is much room for discovery in the field of thermoacoustics. Optimization techniques as a design aid, for example, are severely under-utilized, and previous efforts in thermoacoustic optimization are rare. Minner et al. consider the optimization of a thermoacoustic refrigeration system. This work uses extensive model development and seeks to optimize the coefficient of performance. The group considers geometric parameters and fluid properties of the system and a simplex algorithm to search for the optimal solution. However, in order to account for the thermoacoustic operating conditions, DeltaE is used extensively [13]. Both Wetzel and Besnoin discuss optimization of thermoacoustic devices in their work. Wetzel targets the optimal performance of a thermoacoustic refrigerator, Besnoin targets the heat exchangers [14] and [15], respectively.

In addition to these optimization efforts, parametric studies have been utilized to estimate the effect of single design parameters on device performance. Zoontjens illustrated the optimization of inertance sections of a thermoacoustic devices. Upon closer inspection, they used DeltaE to vary individual parameters to determine optimal designs [16]. Ueda also determined the effect of a variation of certain engine parameters on pressure amplitudes [17]. Tijani et al. attempted to optimize the stack spacing; however, they also utilized DeltaE for this work [18]. This is by no means a complete list of the "optimization" of engine components, but it is a good overview of optimization targets. Each work is undoubtedly a valuable addition to the thermoacoustic community, but they should not be considered optimizations in the classical sense, but rather parametric studies. In all likelihood, each "optimal" design is a local optimum as the optimization performed by each group considers one variable and all else equal.

One common trait of all previous optimization efforts is that thermal losses to the surroundings that occur in the operation of the devices are not considered. In reality, however, we can optimize a thermoacoustic device with regard to one of the following objectives:

1. Power output,
2. Heat input,
3. Viscous losses in the individual channels, and
4. Heat loss through the device boundaries and cooling medium.

It is intuitive that an increased heat input may increase the power output, but as a result, it may also increase the heat losses. It is the goal of this work to illustrate these tradeoffs, as they are not understood in detail. Below, an estimate of the magnitude of these thermal losses will be provided. It shows that these losses are significant when compared to total heat input and should be considered as a design criterium.

1.4. Motivation

Considering a simple thermoacoustic engine, comprised of a stack inside of a resonance tube, the energy flows are obvious. One side of the stack is heated, while the other side is cooled. As a result of this heating, strong pressure oscillations are created, which is the expected output of any thermoacoustic engine. However, as a secondary result of this heating, we must consider the thermal losses in the stack region of the engine. All three heat transfer modes are present: convection, radiation and conduction. Below, an estimate of the magnitude of said energy losses is performed. The values of each parameter discussed are derived from measurements from a simple demonstration engine as shown above in Fig. 1. During these measurements, the electrical power supplied to the ceramic stack was increased until oscillations occurred. At the onset, it was recorded that the hot side temperature was 306 °C and the cold side (uncooled, facing ambient air) showed a temperature of 50 °C. The applied voltage was 15.1 V.

With a known resistance of the heating wire, an input power of approximately 50 W can be calculated. Given an outer diameter of the glass tube that houses the stack, and a uniform temperature distribution across the entire cross section of the stack and tube, and a total length of 20 mm over which this temperature difference is applied, we can calculate a convective heat loss (free convection, using a temperature dependent Nusselt number) of 4.7 W. In addition, we have to consider a radiative heat loss as well. Using the surface coefficient of emission provided in the pyrex data sheet ($\varepsilon_{\text{Pyrex}} = 0.85 \ldots 0.95$), this radiative heat loss can be estimated to be approximately 5.1 W. This estimate shows that the heat losses, for the case of the demonstrator engine, are significant relative to the total energy supplied to it. This provides the motivation to optimize the geometry of the stack. There are obvious tradeoffs between the length of the stack and the circumference of the tube that houses the stack. It is intuitive that an increased heat input may increase the power output, but as a result, it may also increase the heat losses.

The magnitude of the thermal losses leads us to consider them as a design criterium for thermoacoustic devices. As a starting point this work target a thermoacoustic engine. These systems provide a simple geometry to demonstrate the feasibility of our methodology. TAEs will ultimately be applied in TAR systems to achieve refrigeration with no moving parts, which will undoubtedly increase system complexity and the modeling efforts. For future thermoacoustic systems designs, the thermal losses should be taken into account, especially with regard to the miniaturization of thermoacoustic devices. As the overall size shrinks, the surface area to (active) volume of a thermoacoustic engine, for example, increases, which in turn leads to higher thermal losses. This work aims to highlight one methodology to incorporate thermal losses in a design process by combining the fields of thermoacoustics and optimization.

2. Model development

The challenge in this work was to account for the temperature distribution throughout the stack in an accurate way. The solution to a three dimensional heat conduction problem subject to convective and constant temperature boundary conditions requires significant efforts [19]. For our initial model, only the stack geometry is considered; the model does not consider any variation in operating condition or the interdependency of stack location and performance.

2.1. Computational domain

Because of the symmetry present in the stack, the problem can be reduced to a two dimensional domain, with two constant temperature boundaries, one convective boundary, and finally one adiabatic boundary, as shown in Fig. 2. In order to maintain account for thermoacoustic phenomena, the work flow and viscous resistance occurring in the stack are account for, albeit in basic form.

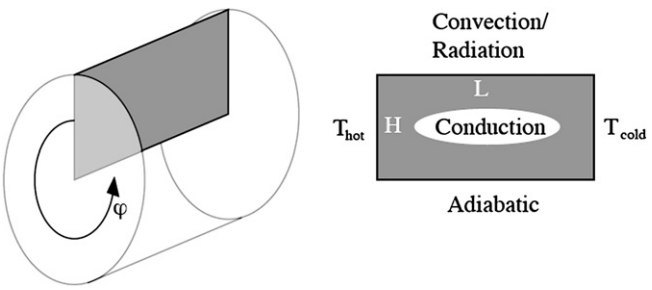

Fig. 2. Illustration of computational domain and implemented boundary conditions.

The temperature distribution throughout the rectangular domain was calculated using COMSOL Multiphysics, a finite element solver. The simple geometry allowed for straightforward computations when building and meshing the domain as well as solving for the temperature distribution. In order to consider all relevant energy fluxes correctly, the resulting outer surface area as well as the face areas have to be calculated by integrating over the angular component (defined as φ) of the cylindrical coordinates. In addition to calculating the temperature distribution in the stack efficiently, COMSOL also allows for integration into Matlab, which is important for the ensuing optimization, where the domain size was varied repeatedly.

The rectangular representation of the stack was meshed using triangular cells. As the domain size will be varied over the course of the optimization, we have to maintain equal cell density for all domain sizes. Thus, the cell size was chosen to be constant for all domains used (i.e. fixed cell count per unit area). The cell type was chosen to be Lagrange quintic in order to minimize numerical errors. Lower order cell types caused some instability in the temperature solution throughout the domain as a result of the transition from initialized distribution to the physical distribution as the calculation progressed.

2.2. Boundary conditions

The boundary conditions on the modeled rectangle are prescribed as follows (left vertical wall as number 1, going counterclockwise):

1. Constant temperature (T_{hot}),
2. Adiabatic boundary, modeling the axis of the cylindrical stack,
3. Constant wall temperature (T_{cold}), and
4. Free convection and radiation to surroundings (at T_∞), with a temperature dependent heat transfer coefficient.

The material properties of the solid are assumed to be constant. The temperature of the domain is initialized to 300 K. The channels of the stack are not modeled explicitly, but they are accounted for by assuming an anisotropic thermal conductivity.

2.3. Anisotropic thermal conductivity

In order to account for the anisotropic nature of the stack as a result of the channels, the model was given two different thermal conductivities, one for the axial direction (open channels and solid in parallel), and one for the radial direction (open channels and solid in alternating series). COMSOL allows for anisotropic material properties in the form of

$$\mathbf{k} = \begin{pmatrix} k_{xx} & k_{xy} \\ k_{yx} & k_{yy} \end{pmatrix} \tag{2.1}$$

With this option, we can derive an advanced description of the stack without actually modeling the channels individually. As a basis, we consider the bulk thermal conductivity of the solid material being used, in addition to the channel size with the gas' thermal conductivity for the net cross-channel thermal conductivity. Only the values for axial and transverse thermal conductivity k_{xx} and k_{yy} are of interest. They can be calculated as shown in Equations (2.2) and (2.3):

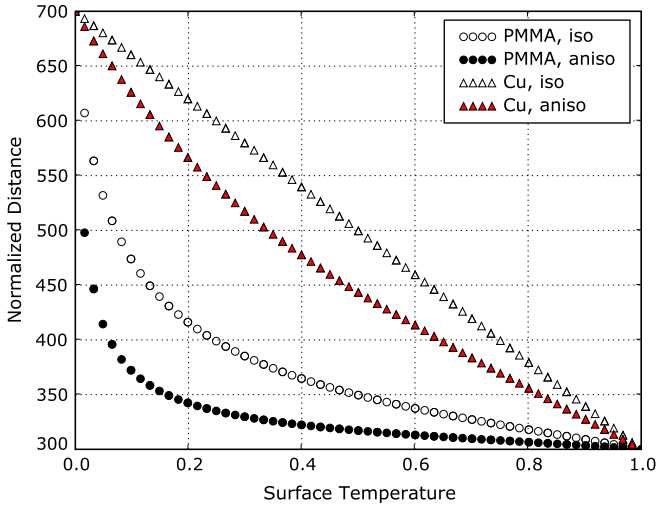

Fig. 3. Temperature differences between isotropic and anisotropic thermal conductivity for Copper and PMMA, $L \times H = 0.4 \times 0.2$.

$$k_{xx} = \frac{t_w k_{solid} + d_c k_{gas}}{t_w + d_c} \tag{2.2}$$

$$k_{yy} = \frac{k_{solid} k_{gas} (t_w + d_c)}{k_{solid} d_c + k_{gas} t_w} \tag{2.3}$$

In order to show the influence of the anisotropic material properties, we evaluated the temperature field in the rectangular domain for two different materials (copper and polymethyl methacrylate (PMMA)), in order to show two different extremes of bulk thermal conductivity. Fig. 3 shows the results.

3. Objective functions

With the computational domain defined, the objective functions can now be developed. In the present work, these are the conductive heat flux from the stack's outer surface, the conduction through the stack as well as acoustic work and viscous resistance.

3.1. Convective and radiative heat flux

In the introduction, we have illustrated the magnitude of the convective heat flux from the outer surface of the stack to the surroundings in order to provide a motivation for this work. There, a linear temperature profile was used to estimate the heat transfer coefficient and the heat flux to the surroundings. In this model, however, the actual temperature distribution throughout the stack is be taken into account by utilizing COMSOL, as we account for a temperature dependence of the heat transfer coefficient. For the solid portion of the stack, these considerations assume bulk material properties that are independent of temperature. The convective heat transfer coefficient and the radiative heat flux to the surroundings are assumed to be dependent on the temperature. The total convective heat transfer across the cylindrical shell in its integral form can be described by:

$$Q_{conv} = H \int_0^{2\pi} \int_0^{L} h(T(x))(T(x) - T_\infty) \mathrm{d}x \, \mathrm{d}\varphi. \tag{3.1}$$

The heat transfer coefficient h is derived from the Nusselt number, which is a non-dimensional heat transfer coefficient. It is shown for the case of a horizontal tube subject to free convection [20]:

$$\mathrm{Nu} = 0.36 + \frac{0.518 \mathrm{Ra}_D^{\frac{1}{4}}}{\left[1 + \left(\frac{0.559}{\mathrm{Pr}}\right)^{\frac{9}{16}}\right]^{\frac{4}{9}}} = \frac{h D_{char}}{k_{gas}} \tag{3.2}$$

This expression depends on the Prandtl number, a characteristic dimension D_{char}, which is the lateral domain dimension H in this case, and the Rayleigh number, which in turn can be expressed by:

$$\mathrm{Ra} = \mathrm{Gr}\,\mathrm{Pr} = \frac{g\beta(T - T_\infty)H^3}{\nu\alpha} \tag{3.3}$$

where Gr is the Grashof number, Pr is the Prandtl number, T is the surface temperature, $T_\infty = 300$ K is the (constant) temperature of the surroundings, ν is the viscosity of the surrounding gas, and α is the thermal diffusivity of the surrounding gas (air). Like all Nusselt number correlations, it is an empirical expression for this specific case of heat transfer. In order to derive the actual convective heat transfer coefficient, the Nusselt number is multiplied by the thermal conductivity of the surrounding gas, and divided by the characteristic dimension of the surface under consideration (again, stack radius H in this case).

The radiation heat flux becomes increasingly important as T_{hot} increases, as shown in Equation (3.4):

$$Q_{rad} = H k_B \int_0^{2\pi} \int_0^{L} \varepsilon \left(T(x)^4 - T_\infty^4\right) \mathrm{d}x \, \mathrm{d}\varphi \tag{3.4}$$

The final heat flux objective for the top surface of the domain is the sum of both convective and radiative heat fluxes

$$Q_{obj,1} = Q_{conv} + Q_{rad} \tag{3.5}$$

where k_B is the Stefan Boltzmann constant, and ϵ is the surface emissivity, which depends on the emitted wavelength, and in turn is a function of temperature (an effect that may not be negligible if the temperature difference across the domain is sufficiently large).

3.2. Conductive heat flux

This heat flux is representative of the heat loss across the cold end of the domain. As the temperature gradient there is non-zero, a heat flux must be present. It is assumed that thermal energy is removed via the cooling water flow. Similar to the cylindrical shell, this heat flux has to be integrated over the whole surface representing the cold side:

$$Q_{cond} = Q_{obj,2} = \int_0^{2\pi} \int_0^{H} \left(k_{xx} \frac{\mathrm{d}T}{\mathrm{d}x}\right) \mathrm{d}x \, \mathrm{d}\varphi \tag{3.6}$$

In addition to the thermal energy fluxes inside the stack, we also have to account for energy fluxes that are inherent to thermoacoustic engines. The acoustic power and the viscous resistance expressions are developed below.

3.3. Acoustic power

According to Swift, the acoustic power per channel is given by

$$W = 1/4 \Pi L \omega \left[\delta_\kappa \frac{(\gamma - 1)p^2}{\rho c^2 (1 + \epsilon)} (\Gamma - 1) - \delta_\nu \rho u^2 \right] \tag{3.7}$$

which is composed of the thermal contribution minus the viscous effects [4]. Π is the channel circumference, ω is the operating frequency, γ is the ratio of the specific heats (isochoric and isobaric), ρ is the gas' density, and Γ is the ratio of critical temperature gradient and local temperature gradient, which has previously been introduced with Equation (1.1) [6]. p and u are the pressure and velocity amplitude achieved in the stack. With data taken from the engine assembly shown above, the pressure amplitude in the stack is assumed to be $p_{\max} = 500$ Pa. With this information, the velocity amplitude can be derived from Equation (3.8), which describes the velocity distribution in a standing wave:

$$u = i \left(\frac{p}{\rho c} \right) \cos \frac{x}{\lambda} \tag{3.8}$$

to be $u_{\max} = p_{\max}/(\rho c) = 1.3\ \mathrm{m\,s^{-1}}$. For this study, both amplitudes are assumed to be constant for all stack geometries and materials. Finally, ϵ is the so-called plate heat capacity ratio [21] and can be expressed by:

$$\epsilon = \frac{(\rho c_p \delta_\kappa)_{\mathrm{gas}}}{(\rho c_p \delta_s)_{\mathrm{solid}}} \frac{\tan h((i+1)y_0/\delta_\kappa)}{\tan h((i+1)l/\delta_s)} \tag{3.9}$$

This expression can be simplified to values of $\epsilon = y_0/\delta_\kappa$ if $y_0/\delta_\kappa < 1$ and $\epsilon = 1$ if $y_0/\delta_\kappa > 1$, where y_0 is half of the channel height, l is half of the wall thickness, δ_s is the solid's thermal penetration depth. As mentioned above, the expression for the work output is provided for a single channel. In order to provide a physical representation and to be consistent with the remaining assumptions, we estimate the total number of round channels N_c as a function of cross section size for the cylindrical stack. For a circular domain, this estimate equals the ratio of overall domain size and cross sectional size of each channel, decreased to 70% of this value to account for the solid percentage of each channel.

$$N_c = \frac{4\pi H_t^2}{\pi d_c^2} 70\% \tag{3.10}$$

An added degree of accuracy would be achieved by determining the actual number of channels by utilizing a packing correlation for square surfaces in a circular domain. For the sake of simplicity, this is omitted.

3.4. Viscous resistance

The viscous resistance for each channel is given by:

$$R_\nu = \frac{\mu \Pi L}{A_c^2 \delta_\nu} \tag{3.11}$$

where Π is the circumference and A_c the area of the channel. This expression has the units [kg/m^4 s]. In order to express this in terms similar to the other variables used, we multiply Equation (3.11) by the volumetric velocity [m^3/s] and the oscillating frequency [1/s], yielding [W/m] as a final unit for the viscous resistance per channel. Just as the total acoustic power of the stack was dependent on the total number of channels, the viscous resistance also depends on this value. As the full stack represents a network of parallel resistances, we divide the value for the individual resistance by the same factor N_c derived above for the acoustic power. Below, we describe how the objective functions are conditioned and implemented in the optimization routine.

4. Solution strategy

Since we are attempting to find a geometric optimum of the stack geometry, the radius and length of the stack have to be varied as part of an optimization loop. Each time, the temperature distribution has to be calculated. The overall process can be summarized as follows:

1. Initial guess for domain dimensions,
2. COMSOL solution for temperature distribution and heat fluxes,
3. Matlab evaluation of the objective and penalty functions, and
4. Repeat if not optimal, else terminate.

4.1. Normalizing objective functions

The objective functions as introduced above in Section 3 are given in a general form, all with different units and also different orders of magnitude. This would result in skewed results from the optimization as the optimizer considers all objectives as a sum. For this reason, all objectives have to be scaled as to provide dimensionless values that are on a similar scale.

4.1.1. Normalizing the work output and viscous resistance

The maximum work output is always achieved when the domain size is maximized. This is obvious, both because the larger the cross section of the stack, the more channels it can hace, and because there is a linear relationship between power and stack length. Thus, the maximum work output is achieved at the maximum allowable length and cross section, multiplied by the open area coefficient, as defined in Equation (3.10), as shown in Equation (4.1):

$$W_{\max} = N_c|_{H_{\max}} \frac{\delta_\nu \delta_\kappa (\Gamma - 1)\omega p_{\max}}{\rho c^2 (1 + \varepsilon)} \left(\frac{\nabla T}{\nabla T_{\mathrm{crit}}} - 1 \right) \tag{4.1}$$

All parameters used here are the same as introduced above in Equation (3.7). For the viscous resistance, the maximum value is achieved with the longest channel, as this provides the most surface area and thus the highest viscous loss (Equation (4.2)). The maximum total resistance is achieved at the smallest tube cross section, because it can incorporate the smaller number of channels (which is accounted for by the factor $N_c|_{H_{\min}}$, in Equation (4.3)).

$$R_{\nu,\max,c} = \frac{\mu \Pi_{\min} L_{\max}}{A_{c,\min}^2 \delta_\nu} = \frac{4\mu \delta_\nu L_{\max}}{\delta_\nu^2 \delta_\nu} = \frac{4\mu L_{\max}}{\delta_\nu^2} \tag{4.2}$$

$$R_{\nu,\max} = 1/N_c|_{H_{\min}} R_{\nu,\max,c} \tag{4.3}$$

The work output and resistance expressions thus depend only on terms that are constant, and simple terms that depend solely on domain dimensions. For this reason, the normalization of both objectives is straightforward:

$$\mathrm{Obj} = \frac{\mathrm{value}}{\mathrm{max.value}} \tag{4.4}$$

4.1.2. Normalizing the heat flux

In the case of the heat fluxes, the normalization is less straightforward, as it is not immediately clear where their

maximum and minimum values are achieved. For this reason, a separate COMSOL calculation is performed, evaluating all heat fluxes for all possible combinations of domain dimensions that are allowed within the imposed boundaries on the domain (L_{min}, L_{max}, H_{min}, H_{max}). This domain is discretized with a separate grid, and all heat flux values are calculated and stored in a matrix. The respective maximum and minimum values of this matrix are then used to normalize the heat fluxes according to Equation (4.5):

$$\text{Obj} = \frac{\text{value} - (\text{min.value})}{(\text{max.value}) - (\text{min.value})} \tag{4.5}$$

With these normalization schemes in place, all objectives vary between 0 and 1, and both values are achievable within the domain. This allows us to optimize with respect to their sum, as the system is dimensionless and all four objectives are now on the same order of magnitude. In order to provide bounds on the variables used in this study, we implemented the following penalty functions.

4.2. Penalty functions

Two penalty functions are used for each decision variable (for the upper and lower bounds). For example, we want to avoid solutions such as the long and thin stack (“pencil” shape) or the short and large-radius stack (“disc” shape). The penalty functions are only evaluated if the variable is actually violating the boundary, otherwise they assume a value of 0.

In our current case, the variables that need to be constrained are the axial and radial dimensions of the rectangular domain, L and H, respectively. They take the same format for both variables:

```
if H_min − H > 1e−12
penalty = 10 + (H_min − H) * 1e8
end
    and
if H − H_max > 1e−12
penalty = 10 + (H − H_max) * 1e8
end
```

As soon as the constraint is violated, the constant term of the penalty ensures an immediate effect on the border of the feasible region, while the linearly increasing term ensures that the algorithm will avoid solutions further away from the feasible region. $H_{min} - H > 1e{-}12$ rather than $H_{min} - H > 0$ is used as a check for violation, as 0 is not well defined in numerical terms. The latter check could lead to numerical instabilities. In order to still provide a reasonable gradient as the domain violation becomes more severe, the difference $H_{min} - H$, and similarly for a violation of $H - H_{max}$ is multiplied by a large constant. The summation of the normalized objectives and the penalty functions form the total objective function F_{obj} as illustrated in Equation (4.6).

$$\text{minimize } F_{obj} = \sum_i w_i f_{obj,i} + \sum_i p_i \tag{4.6}$$

where p_i represent all penalty functions, and w_i is used to weight the individual objectives. The weighting factors can be used to shift the design emphasis on, say, the convective heat flux, or on work output, for example.

It can be shown that unconstrained optimization using penalty functions can yield the optimal solution of the original objective if the penalty imposed on the new auxiliary function (which is the combination of primal function and the penalty) is sufficiently large. On the other hand, a penalty that is too large can lead to problems when trying to solve the optimization problem; the problem can become ill-conditioned [22]. Consequently, the penalty function has to assume a value of 0 when the design constraints are not violated, and large if a bound is violated. The following sections will elaborate on the derivation of the objective functions and the penalty functions specific to this problem.

4.3. The optimization method: Nelder–Mead simplex

The Nelder–Mead search algorithm in a d-dimensional space uses $d+1$ points to determine a downhill direction of an objective function. It does not rely on gradients, and thus the function does not have to be differentiable for the algorithm to be successful. For a surface, the algorithm uses three points (corners of a triangle), evaluates the function values and then applies one of four moves to the worst point: reflection, expansion, contraction, and shrinkage. The simplex changes its shape, and the one new function value is evaluated and compared to the one it has replaced. Based on the behavior of the function value from one iteration to the next, the algorithm chooses which modification to apply [23]. The algorithm uses an initial guess as input, and then varies the variables according the simplex function values. In the current case, it will vary both axial and lateral dimensions of the used rectangular domain. The hot side temperature is estimated before the first iteration based on the axial domain dimension and a given bulk temperature gradient. Locally, this temperature gradient varies significantly as the heat flux across the top surface is included (as calculated by COMSOL).

5. Implemented optimization routine

As introduced above, the optimization requires that we know the maximum possible value of each of the four objectives. For this reason, a preprocessor is implemented that utilizes COMSOL to calculate the heat fluxes across the top and cold surfaces for all possible domain permutations. The feasible reason is subdivided into a grid of L,H points and at each node, the objective functions are evaluated. The result is a matrix of objective function values as a function of both L and H.

```
given Lmax, Hmax
i,j = 1
for i = 1:stepsize
    for j = 1:stepsize
        L = i * Lmax/stepsize
        H = j * Hmax/stepsize
        objective(i,j) = COMSOL calculations (L,H)
    end
    j = 1
end
return objective
```

This solution routine is shown graphically in Fig. 4. First, we calculate the extrema of the objectives that can be reached given a set of allowable domain dimensions. Function 1 (F1) passes this information into COMSOL where the temperature distribution for each case is calculated. As a result, we determine the work output, viscous resistance and the heat fluxes that correspond to each of the extreme domain sizes. This information is stored in a file.

Next, we define a vector $\mathbf{v}_0$ that contains the initial guess for variables L and H. fminsearch passes this information into

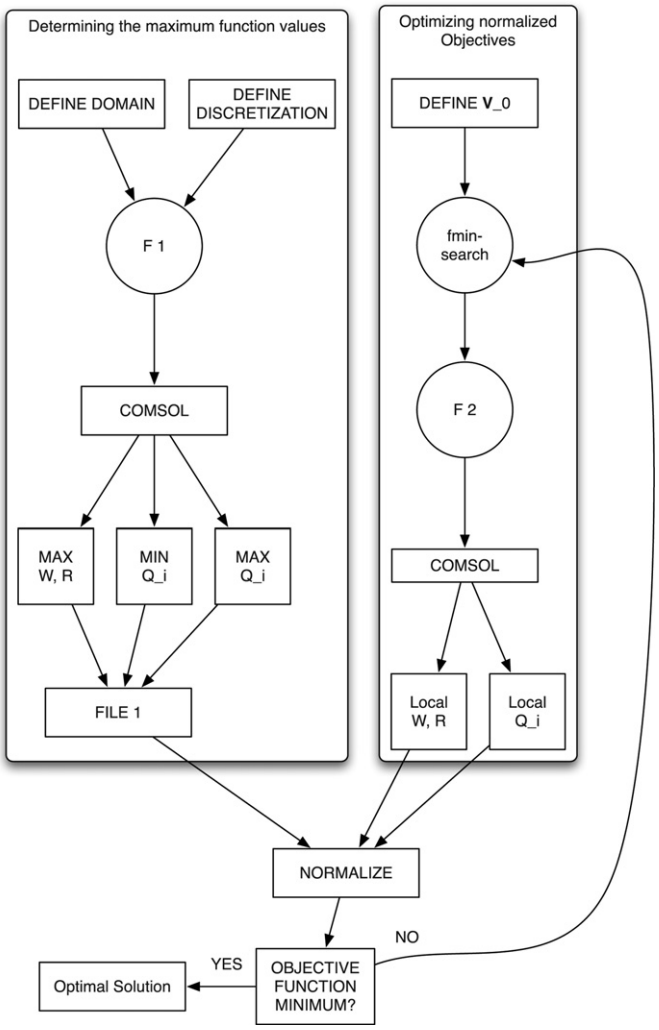

Fig. 4. Flow diagram of the optimization routine, including the preprocessor.

Function 2 (F2) which in turn calls COMSOL to perform temperature calculations for the specific domain. As a result, the "local" work output, resistance and heat fluxes are calculated. The values for the extrema calculated before are read from the file and used to normalize the objectives. If the algorithm determines that the current solution is optimal, it terminates the process, otherwise, it derives a new guess for domain dimensions which is passed back into the algorithm.

5.1. Mesh dependence of the solution

We conducted a sensitivity analysis in regard to the heat flux through the top surface of the domain (subject to convective heat flux). The mesh was refined in 5 steps, increasing the cell count by a factor of approximately 4 each time. The initial mesh contained 516 cells. The largest mesh that COMSOL was able to solve contained over 132,000 cells. We found that relative to the total value of the heat flux, the error resulting from the coarse mesh is approximately 2%. Fig. 5 shows a plot of the heat flux post-processing data versus used mesh size. It shows that the step improvement is leveling off, thus a further increase of error can be assumed to be negligible.

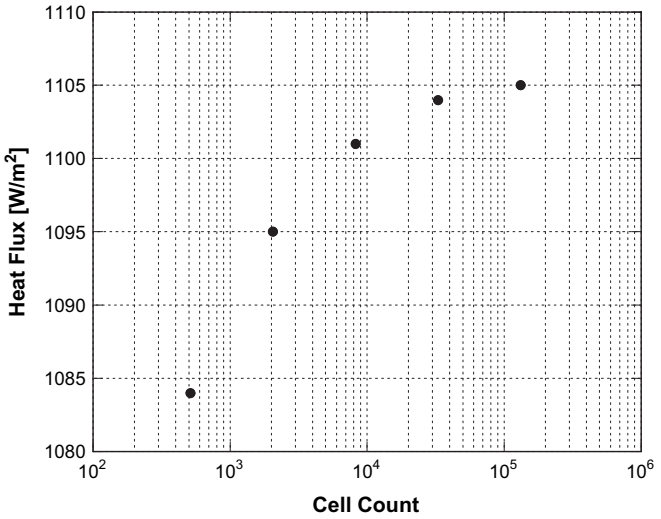

Fig. 5. Illustration of the error resulting from using a coarse mesh rather than a refined mesh in COMSOL. The error is less than 2% and not expected to rise further with increasing cell count.

Table 1
Sensitivity analysis for the grid size during the calculations of maximum values of heat fluxes.

Discretization	$Q_{top,\ max}$	$Q_{top,\ min}$	$Q_{out,\ max}$	$Q_{out,\ min}$	Sol'n time
5×5	174.6	6.88	65	0.003	Approx. 5 min
10×10	174.6	6.83	65	0.003	Approx. 10 min
20×20	174.6	6.62	65	0.003	30 min
40×40	174.6	6.4	65	0.003	90 min

5.2. Pre-processing accuracy

Pre-processing for the optimization calculates all possible values for work output, resistance, and heat fluxes in the feasible domain. Their values are dependent on the domain dimensions, where all other previously mentioned parameters (such as channel size, and temperature gradient) are assumed to be constant. This allows for visualization of the results using surface and contour plots. The calculation of the normalized heat fluxes requires COMSOL to be executed twice for each combination of domain width and height. This is very resource intensive,[1] and can severely slow down the entire process, especially when considering that the optimization is for only two decision variables. The optimization (the right hand side of Fig. 4) only requires one COMSOL evaluation. The hardware used is a computer equipped with a 3.2 GHz Pentium 4 processor, using 2 GB of RAM. This sensitivity analysis was done with grids of 5×5, 10×10, 20×20, and 40×40 cells. The domain sizes were kept constant. The results are shown in Table 1.

The sensitivity analysis in regard to the pre-processing and determination of the respective extreme values of the heat fluxes calculated by COMSOL shows that there is very little variation when the discretization of the grid is changed. This is because the functions for the heat fluxes are monotonic, and their maxima and minima occur on the boundary where L and H are at extrema as well. This is an important discovery, and could not have been assumed before doing this evaluation.

[1] A discretization of 40×40 cells requires 1600 COSMOL evaluations.

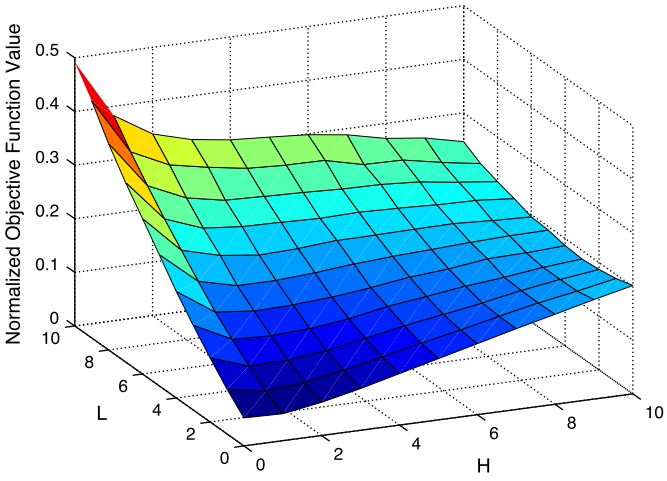

Fig. 6. Objective Function as a function of domain dimensions for PMMA.

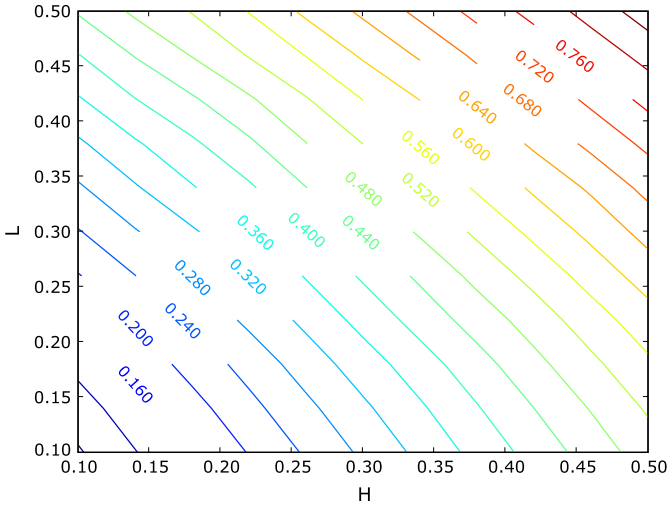

Fig. 8. Contours for Case 5: Emphasis on the Heat Flux Objectives (Convection and Conduction).

6. Results

The feasible domain for a thermoacoustic stack is defined as 0.1–0.5 m. This range is large, but was chosen in order to illustrate the behavior of the objective functions outside of the "practical" range. The results are presented in the form of contour plots of the objective function and a variation of the stack material, a variation of the initial guess (for constant material and weights), and finally a variation of the weights for each of the four objectives.

6.1. Shape of the objective function

As a result of the preprocessor, we can determine the overall shape of the objective function. Since it is only dependent on two parameters, it can be illustrated using a surface plot. One of these plots is shown in Fig. 6. This figure represents the objectives weighted equally at 25% each.

In order to provide more insight in the behavior of this function depending on the material used for the stack, we ran this optimization for five additional (feasible) materials. The physical properties of the materials used are given in Table 2.

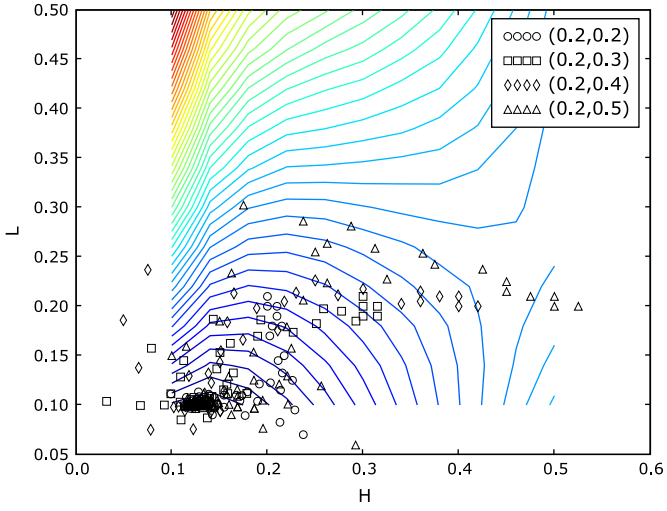

Fig. 7. Behavior of the Optimization as a function of initial guess.

These results are given in the Appendix in Fig. 9. The overall trend is the same regardless of material, but we can notice slight variation in the shape of the objective function. The highly thermally conductive materials (aluminum and copper) are shown to be more sensitive to a variation in stack dimension than the alternative materials.

6.2. Optimization behavior

The behavior of the optimization routine can be shown when we consider a contour plot of the objective function and plot the domain size for each function call. This result is shown in Fig. 7. This shows how the optimizer changes the domain variables for each iteration step for different initial guesses (constant L, H varying). Because of the shape of the objective function in the area of the initial guesses, the solution converges to the same combination of L and H for each case. Fig. 10 in the Appendix illustrates additional cases of this analysis.

6.3. Varying the weights

For the PMMA[2] case, we varied the weights, all cases highlighting emphasis on one objective or a group of objectives (power and resistance is one group, the heat fluxes another group). Table 3 shows the weight distribution for all cases.

Fig. 8 shows the case for an emphasis on just the heat loss via convection and conduction (Case 5). Multiplied by the open area coefficient, as defined in Equation (3.10). We can see that in order to minimize the heat losses, we must design the stack to be as small as possible. In addition of only focussing on the heat losses, we also investigated other weight distributions. The corresponding contour plots are shown in Fig. 11 in the Appendix. For example, disregarding the thermal losses completely, the emphasis on an increased height (that is greater cross sectional area of the stack) is apparent. Emphasizing solely on power, the design is required to be as large as possible (keeping in mind that in this case, the objective is to minimize *the negative value*).

[2] The tendencies revealed for PMMA are very similar for all other materials considered.

Table 2
Properties of the materials used in the material variation.

Material	Density [kg/m^3]	Heat capacity [J/kg K]	Thermal conductivity [W/mK]
Aluminium	2700	900	160
Copper	8700	385	400
Titanium	4940	710	7.5
Steel	7850	475	44.5
PMMA	1190	1420	0.19
SiO_2	220	730	1.4

Table 3
Weight distribution (in %) for all objectives, corresponding to Fig. 11.

Case	Acoustic power	Resistance	Conv. heat flux	Cond. heat flux
1	70	10	10	10
2	10	70	10	10
3	10	10	70	10
4	10	10	10	70
5	0	0	50	50
6	50	50	0	0

7. Discussion and conclusions

We have developed a basic model of a stack as part of a thermoacoustic engine. This model is built in order to develop an understanding of the importance of the thermal losses encountered in the operation of thermoacoustic engines. As a design supplement, we included the calculation of the heat fluxes into an optimization routine, a method that is currently underused in thermoacoustics. In order to illustrate a dependency on the stack bulk material, we provided results for several different feasible stack materials.

7.1. Discussion

The surface plots for all materials show that the objective function is not convex. For this reason, there are several local optima but from a visual inspection, only one global optimum. It is obvious that the total length is always decreased to its imposed minimum value. The penalty functions keep this boundary from being violated. This location corresponds to a mechanically feasible design as it shows that the radius of the stack should be roughly 20% larger than the length of the stack (again, provided the designer weighs all objectives equally). As a result of the material variation, we can identify slight changes in the absolute values of the objective function, but not a drastic change in the general tendencies and shape. The ideal design remains at the smallest value for L and a slightly larger value for the radius.

The illustration of the optimization behavior showed all combinations of L and H that fminsearch considered. It shows that for most starting points, the area of the minimum objective value was reached. For starting points that were in the plateau regions of the objective function, fminsearch was not able to reach this global optimum, which should be a result of limited step size. For large initial values of L and D, the optimization found the other "optimum" which would result in as large a design as possible. This is, again, rooted in the limited initial step size.

The variation of the weights for each objective shows how the design would change if emphasis is given to one objective in particular, for example as much power while essentially ignoring all losses. In this case, the result showed that as large a design as possible is the solution (which we could have derived from investigating the function for power in Equation (3.7). A more interesting derivation is the design with an emphasis on avoiding the convective/conductive heat loss or the conductive heat loss (and the combination of both) which can be interpreted as "as small as possible." The following design criteria can then be deduced:

- Design as small as possible to minimize thermal losses;
- Increase overall stack radius to increase power output, at cost of higher thermal losses, with optimum at about $H \approx 1.2L$;
- Design as large as possible to maximize power output.

Obviously, choice 1 and choice 3 are conflicting. This illustrates the tradeoff that we have to consider when designing a thermoacoustic engine. Ultimately, it is a personal choice whether to emphasize the thermal behavior or the acoustic behavior. In closing, we will now elaborate briefly on how to improve the current optimization scheme in order to provide more general design information.

7.2. Conclusions

The presented results are a good first approach to using optimization principles in the design of thermoacoustic devices. Considering four objectives simultaneously has shown that for a given length, there is an optimal diameter that results in the least amount of heat loss across the boundary surface and through the cooling water (that is for the case of equal weights given to all four objectives). We have determined a design statement for a driving stack of a thermoacoustic engine. In the future, this work has to be expanded to include thermoacoustic refrigerators, as this technology is the primary application of thermoacoustics with the most potential impact.

In order to fully represent a thermoacoustic system, we have to consider the phasing relationship between pressure and velocity and its impact on heat transfer. This would result in an added influence of the channel size, which is currently assumed to be a constant. The effect of delayed heat transfer, which, with regard to standing wave engines, is an important influence, is neglected. In standing wave engines, the heat transfer from gas to solid has to be delayed in order to achieve the correct phasing between pressure and velocity oscillations. This delay is shorter the smaller the channel is. If the channel size is equal to or less than the thermal penetration depth, there is ideal contact, i.e. no delay in the heat transfer. Ultimately, a consideration of acoustic theory and improved models of thermoacoustic work and loss mechanisms have to be included.

Acknowledgements

This work was supported through the NSF East Asia and Pacific Summer Institute 2008 (OISE-0812781).

Appendix

Plots corresponding to the material variation

The following surface plots illustrate the effect of the variation of the material used for the calculations in COMSOL. This is a combination of all four objectives, with equal weights of 25%. For the materials with smaller thermal conductivity, the objective function is more flat than for the metal cases.

Plots showing the behavior of "fminsearch"

This plot illustrates the behavior of the optimizer for different starting points. Each of the five cases shows different starting points for a constant domain length L. The material used in PMMA, and the objective function is shown as a contour plot.

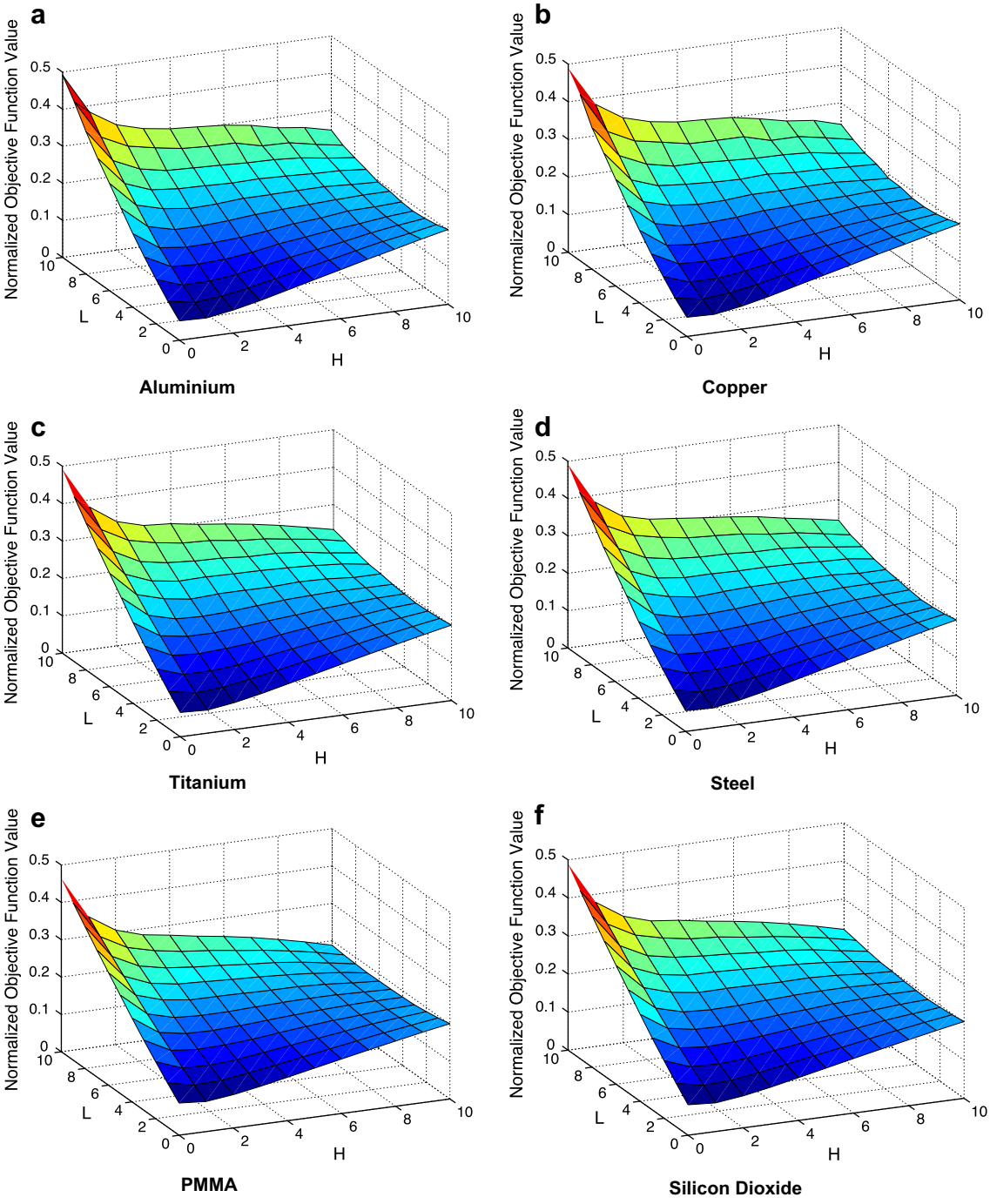

Fig. 9. Variation of the stack material.

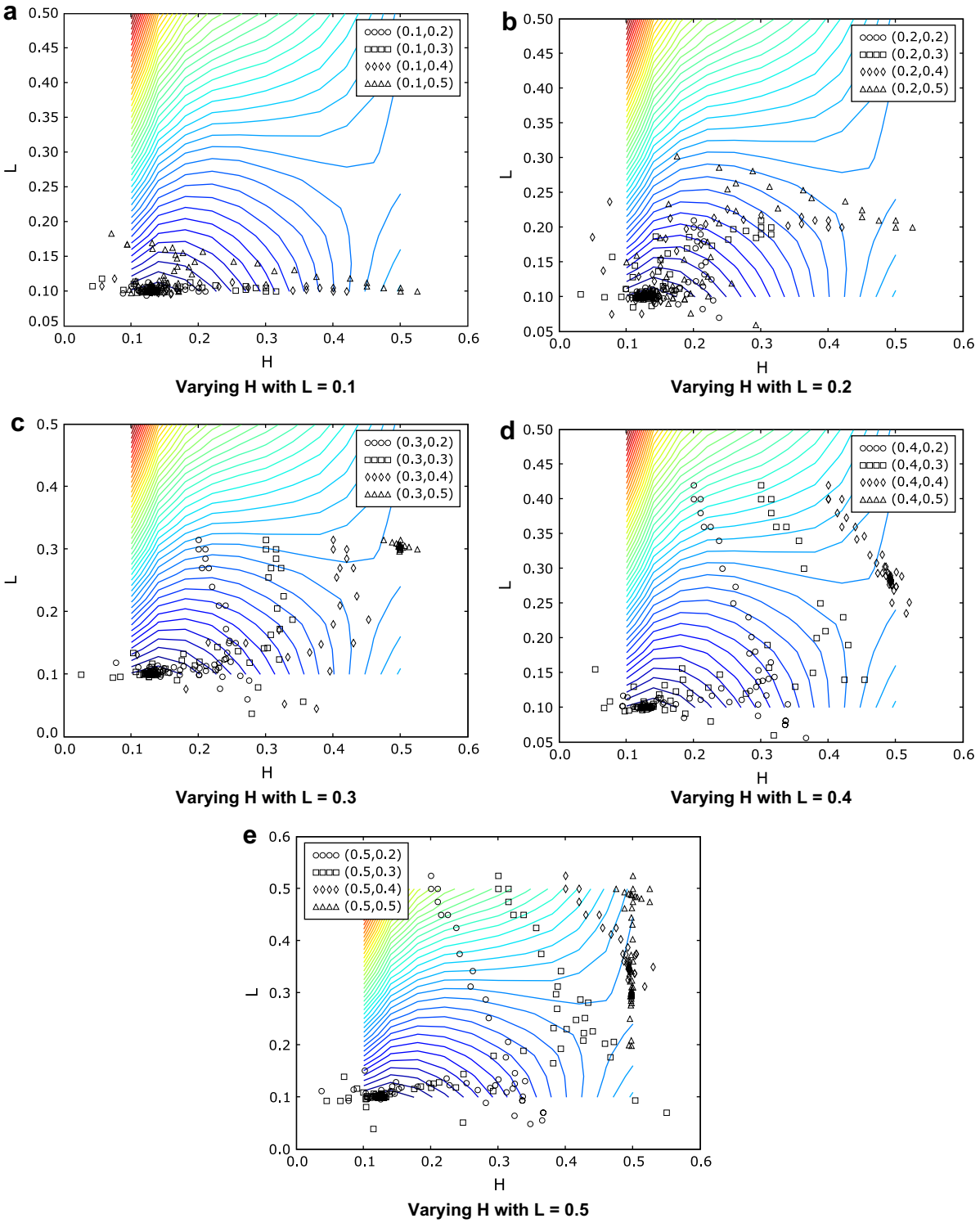

Fig. 10. Variation of the starting points for constant *L* each (Material PMMA).

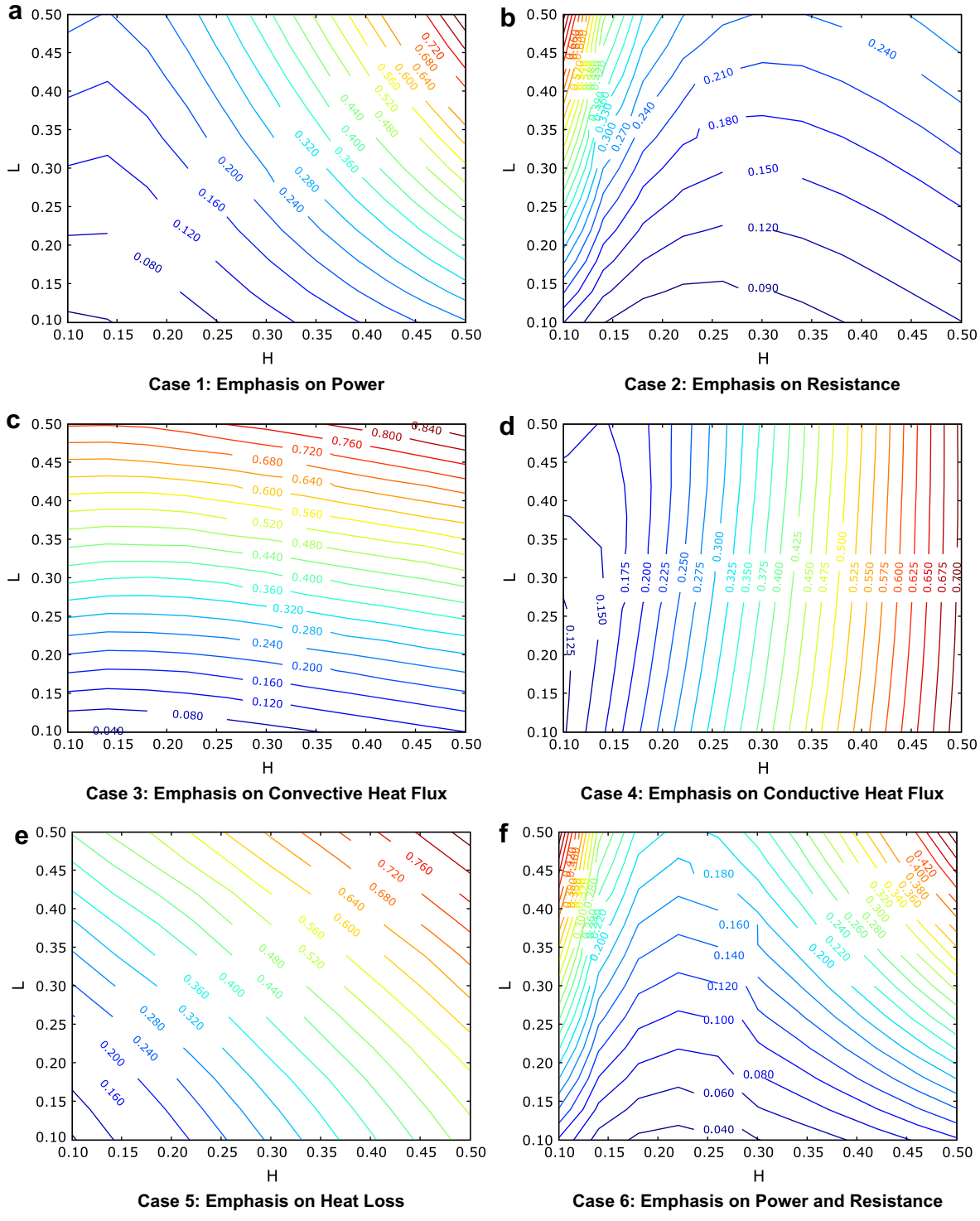

Fig. 11. Variation of the weights for each objective.

References

[1] S.L. Garrett, Reinventing the engine, Nature 339 (1999) 303–305.
[2] S.C. Kaushik, S. Kumar, Finite time thermodynamic analysis of endoreversible Stirling heat engine with regenerative losses, Energy 25 (2000) 989–1003.
[3] P.H. Ceperley, Gain and efficiency of a short traveling wave heat engine, Journal of the Acoustical Society of America 77 (3) (1985) 1239–1244.
[4] G.W. Swift, Thermoacoustics: A Unifying Perspective for Some Engines and Refrigerators, Acoustical Society of America, Melville, NY, 2002.
[5] J.H. Xiao, Thermoacoustic heat transportation and energy transformation, part 3: adiabatic wall thermoacoustic effects, Cryogenics 35 (1) (1995) 27–29.
[6] G.W. Swift, S.N. Backhaus, D.L. Gardner, Us pat. no. 6032464 (2000).
[7] K.J. Bastyr, R.M. Keolian, High-frequency thermoacoustic-Stirling heat engine demonstration device, Acoustics Research Letters Online 4 (2) (2003) 37–40.
[8] M.E. Poese, R.W. Smith, S.L. Garrett, R. van Gerwen, P. Gosselin, Thermoacoustic refrigeration for ice cream sales, in: Proceedings of 6 th IIR Gustav Lorentzen Conference, 2004.
[9] S. Backhaus, G.W. Swift, A thermoacoustic Stirling heat engine: detailed study, Journal of the Acoustical Society of America 107 (6) (2000) 3148–3166.
[10] P.H. Ceperley, Us pat. no. 4355517 (1982).
[11] S.L. Garrett, The power of sound, American Scientist 88 (6) (2000) 516–526.
[12] N. Kagawa, Regenerative Thermal Machines, International Institute for Refrigeration, Paris, 2000.
[13] B.L. Minner, J.E. Braun, L.G. Mongeau, Theoretical evaluation of the optimal performance of a thermoacoustic refrigerator, in: ASHRAE Translations: Symposia, vol. 103, 1997, pp. 873–887.
[14] M. Wetzel, Experimental investigation of a single plate thermoacoustic refrigerators, Ph.D. thesis, Johns Hopkins University (1998).
[15] E. Besnoin, Numerical study of thermoacoustic heat exchangers, Ph.D. thesis, Johns Hopkins University (2001).
[16] L. Zoontjens, C.Q. Howard, A.C. Zander, B.S. Cazzolato, Modelling and optimisation of acoustic inertance segments for thermoacoustic devices, in: Proceedings of ACOUSTICS 2006, 2006.
[17] Y. Ueda, T. Biwa, U. Mizutani, T. Yazaki, Experimental studies of a thermoacoustic Stirling prime mover and its application to a cooler, Journal of the Acoustical Society of America 72 (3) (2003) 1134–1141.
[18] M.E.H. Tijani, J.C.H. Zeegers, A.T.A.M. de Waele, Design of thermoacoustic refrigerators, Cryogenics 42 (2002) 49–57.
[19] M.N. Özisik, Boundary Value Problems of Heat Conduction, International Textbook Company, 1968.
[20] H.D. Baehr, K. Stephan, Wärme- und Stoffübertragung. (transl: Heat and Mass Transfer), fourth ed. Springer, Heidelberg, 2004.
[21] G.W. Swift, Thermoacoustic engines, Journal of the Acoustical Society of America 84 (4) (1988) 1145–1180.
[22] M.S. Bazraa, H.D. Sherali, C.M. Shetty, Nonlinear Programming, Theory and Algorithms, , In: Series in Discrete Mathematics and Optimization, Wiley Interscience, 1993.
[23] T. Bartz-Beielstein, Experimental Research in Evolutionary Computation, Springer, Berlin, Heidelberg, 2006.